Volume 2 | Number 6 | 14 February 2014 | Pages 1573–1992

Journal of Materials Chemistry A

Materials for energy and sustainability

www.rsc.org/MaterialsA

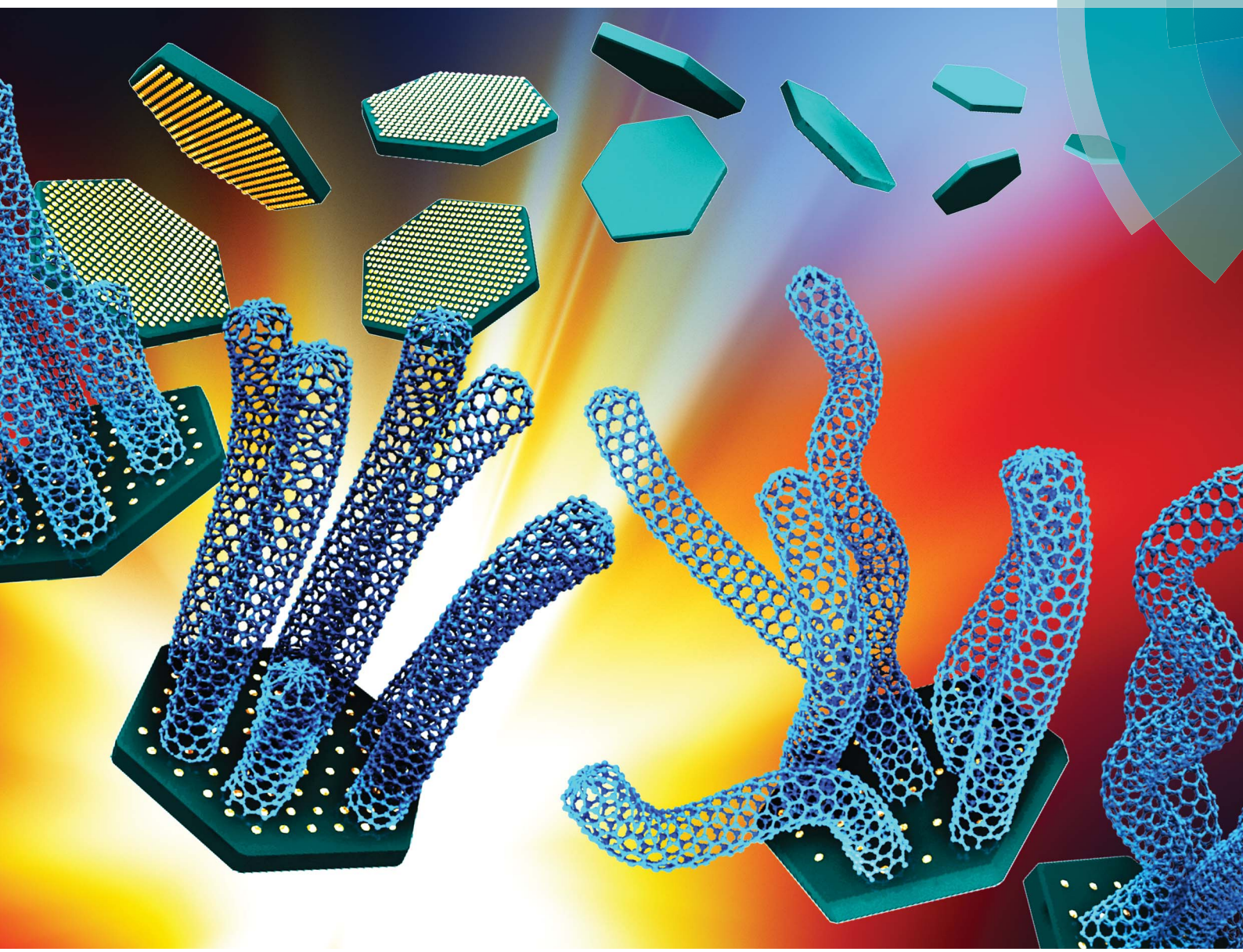

ISSN 2050-7488

ROYAL SOCIETY OF CHEMISTRY

PAPER

Qiang Zhang, Dang Sheng Su, Fei Wei *et al.*

Monodisperse embedded nanoparticles derived from an atomic metal-dispersed precursor of layered double hydroxide for architectured carbon nanotube formation

Journal of Materials Chemistry A

PAPER

Cite this: J. Mater. Chem. A, 2014, 2, 1686

Monodisperse embedded nanoparticles derived from an atomic metal-dispersed precursor of layered double hydroxide for architectured carbon nanotube formation†

Gui-Li Tian,‡[a] Meng-Qiang Zhao,‡[a] Bingsen Zhang,[b] Qiang Zhang,*[a] Wei Zhang,[cd] Jia-Qi Huang,[a] Tian-Chi Chen,[a] Wei-Zhong Qian,[a] Dang Sheng Su*[bc] and Fei Wei*[a]

Received 28th October 2013
Accepted 24th November 2013

DOI: 10.1039/c3ta14380e

www.rsc.org/MaterialsA

Monodisperse metal nanoparticles (NPs) with high activity and selectivity are among the most important catalytic materials. However, the intrinsic process to obtain well-dispersed metal NPs with tunable high density (ranging from 10^{13} to 10^{16} m^{-2}) and thermal stability is not yet well understood. Herein, the preparation of metal NPs with tunable areal density from layered double hydroxide (LDH) precursors in which the metal cations were pre-dispersed at an atomic scale was explored. Large quantities of mesopores induced by the Kirkendall effect were formed on the as-calcined layered double oxide (LDO) flakes. The O atoms bonded with Fe^{3+} cations were easy to be extracted at a temperature higher than 750 °C, which greatly increased the mobility of Fe. Consequently, coalescence of the reduced Fe atoms into large NPs enhanced the Kirkendall effect, leading to the formation of monodisperse embedded Fe NPs on the porous LDO flakes. The flake morphology of LDHs was well preserved, and the areal density of Fe NPs on the LDO flakes can be well controlled through adjusting the Fe content in the LDH precursor. With higher Fe loading, larger Fe NPs with higher areal density were available. When the areal density was increased from 0.039 to 0.55, and to 2.1×10^{15} m^{-2}, the Fe NPs embedded on the LDO flakes exhibited good catalytic performance for the growth of entangled carbon nanotubes (CNTs), aligned CNTs, and double helical CNTs, respectively. This work provides not only new insights into the chemical evolution of monodisperse NPs from an atomic metal-dispersed precursor, but also a general route to obtain tunable NPs as heterogeneous catalysts for chemical and material production.

1. Introduction

Metal nanoparticles (NPs) with high activity and selectivity are among the most important catalytic materials for heterogeneous catalysis for chemical and material production. The metal catalysts have been widely used in large-volume catalytic applications such as Haber–Bosch process for implementation of nitrogen and hydrogen, isomerisation in hydrocarbon cracking for gasoline octane improvement, hydrogenation for manufacture of edible fats and oils, selective oxidation for hydrocarbon derivatives, automobile exhaust conversion for environmental protection, as well as hydrohalogenation for organic synthesis. As heterogeneous catalytic reactions occur only when the reactants are adsorbed onto a working metal surface, the total surface area of metal exhibits an important effect on the reaction rate. It is widely accepted that a higher catalytic activity can be achieved by increasing the surface area of the specific active phase of the catalysts through reducing the size of the corresponding catalytic particles.[1] Consequently, how to disperse the metal NPs with tunable size, high density, and good thermal stability is a great challenge.

In most cases, the monodisperse metal NPs are loaded onto supports by impregnation or co-precipitation. Metal NPs with tunable particle size, shape, and composition are produced in solution through wet-chemistry. Usually, physical barriers, *e.g.*, surfactants,[2] ligands,[3] dendrimers,[4] have to be introduced to separate the metal NPs from each other to prevent their sintering. However, when the as-obtained NPs are employed for catalytic reaction and nanomaterials (*e.g.* carbon nanotubes (CNTs), Au nanowires) synthesis at high temperature, the soft

[a]*Beijing Key Laboratory of Green Chemical Reaction Engineering and Technology, Department of Chemical Engineering, Tsinghua University, Beijing 100084, China. E-mail: zhang-qiang@mails.tsinghua.edu.cn; wf-dce@tsinghua.edu.cn*

[b]*Shenyang National Laboratory for Materials Science, Institute of Metal Research, Chinese Academy of Sciences, 72 Wenhua Road, Shenyang 110016, China*

[c]*Department of Inorganic Chemistry, Fritz Haber Institute of the Max Planck Society, Faradayweg 4-6, 14195 Berlin, Germany. E-mail: dangsheng@fhi-berlin.mpg.de*

[d]*Department of Energy Conversion and Storage, Technical University of Denmark, Risø campus, Frederiksborgvej 399, 4000 Roskilde, Denmark*

† Electronic supplementary information (ESI) available. See DOI: 10.1039/c3ta14308e

‡ These authors contributed equally.

matter based physical barriers have already been removed and the reduced NPs prefer to aggregate into large particles *via* particle migration or Ostwald ripening. The use of other inorganic physical barriers, such as an open shell of support[5] or a meso/nanoporous oxide shell,[1,5,6] increases the thermal stability of very tiny NPs at high temperature. But these physical barriers block the direct contact between the reactants and active sites, which results in the reduced activity of the metal NPs. The use of alloy formation[7] or substrate effects[8] to stabilize metal NPs *via* chemical approaches is also proposed. It should be noted that the materials chemistry to obtain well-dispersed metal NPs with tunable size and high density (ranging from 10^{13} to 10^{16} m^{-2}) and thermal stability at high temperature on an arbitrary substrate is still to be further investigated.

Recently, the use of layered double hydroxides (LDHs) as precursors to produce high-density metal NPs with good thermal stability is highly concerned. LDH is a class of synthetic two-dimensional (2D) nanostructured anionic clays consisting of positively charged layers and charge-balancing interlayer anions. Most of the metals, such as Fe, Co, Ni, Cu, Zn, Mg, Al, Ca, and Li, can be well dispersed in the framework of LDHs at an atomic scale with controllable components. Furthermore, the composition of LDHs can be anticipated for actual catalysts, catalyst precursors, or catalyst supports.[9] Therefore, LDHs are among the most important catalytic materials as multifunctional catalysts and/or precursors for metal-supported catalysts.[10] For instance, phase-pure CuZnAl LDHs have been employed as precursors for Cu rich $Cu/ZnO/Al_2O_3$ catalysts for methanol synthesis[11] and methanol steam reforming.[12] A supported Ni catalyst derived from hydrotalcite is a promising candidate to replace noble metals for hydrogen generation from the catalytic decomposition of $N_2H_4 \cdot H_2O$[13] and landfill gas (main CH_4).[14] The Ni NP catalysts derived from hydrotalcite-like films display high resistance to coke formation and sintering in the dry reforming of methane.[15] The metal NPs reduced from Cu/Zn/Mn/Fe/Al LDHs offer catalytic wet hydrogen peroxide oxidation of phenol; Fe-, Co-, Ni-containing LDHs are excellent catalyst precursors for single-walled,[16] double-walled,[16] multi-walled[17] and (double) helical CNT,[18] CNT/graphene hybrid,[19] and carbon nanofiber[20] formation. The reason for the as-produced metal NPs from LDHs with very high reactivity was considered to lie in the pre-dispersion of metal phases into the LDH flakes at an atomic scale. Recently, our group has reported a chemically mediated precursor induced process in which the metal phases were delicately reduced to form catalyst NPs with high density (10^{14} to 10^{16} m^{-2}), controllable average size distribution (3–20 nm), and extraordinary thermal stability at high temperature (900 °C) from LDH precursors.[21] A family of metal NPs, such as Fe, Co, Ni, Cu, Zn, as well as some noble metals, are able to be reduced into NPs from LDHs with controllable nanosizes, very high densities, and good thermal stability through the guest–host mediated reduction procedure. However, as a core issue for heterogeneous catalysis and materials science, the chemical evolution of ultra-dispersed embedded metal NPs from LDHs is not fully understood yet.

Herein, FeMgAl LDHs were employed to demonstrate the materials chemistry for calcination, reduction, and metal NP formation on LDHs. *In situ* X-ray diffraction (XRD) together with thermogravimetric analysis (TGA), temperature programmed reduction (TPR), and high resolution transmission electron microscopy (TEM) were used to probe the metal NP formation during the calcination and reduction of LDHs. The Kirkendall voids were formed through the different diffusivities of atoms in a diffusion couple after the calcination and the metal NPs were embedded onto or into the layered double oxide (LDO) flakes after the reduction. The size distribution as well as the areal density of metal NPs can be well mediated by adjusting the LDH compositions and reaction parameters. The as-obtained metal NPs were with ultra-high density and exhibited extraordinary catalytic performance for the formation of CNT architectures.

2. Experimental

2.1. LDH synthesis

The FeMgAl LDH flakes were synthesized using a urea assisted co-precipitation reaction similar to our previous reports.[16] LDH-I–LDH-VI were synthesized with the molar ratios of $Fe(NO_3)_3 \cdot 9H_2O : Mg(NO_3)_2 \cdot 6H_2O : Al(NO_3)_3 \cdot 9H_2O$ of (0.05, 0.1, 0.2, 0.4, 0.8, 1.2) : 2 : 1, respectively.

2.2. *In situ* calcination of LDH flakes

In situ XRD was used to detect the structural evolution of FeMgAl LDHs during the calcination and reduction processes. The experiments were carried out in the temperature range of 30–750 °C using a Bruker D8 Advance X-ray diffractometer equipped with a temperature chamber XRK900. The XRK900 chamber is an oven chamber. It is made of stainless steel with Be-windows for X-ray transmission. In the calcination process, the sample and the surroundings were heated at a rate of 0.08 °C s^{-1} in Ar atmosphere (5 mL min^{-1}). Diffraction patterns were recorded at different temperatures, typically at intervals of 20 °C. The sample was equilibrated at any given temperature for 6 min before the scanning with a rate of 8.7° min^{-1}.

2.3. *In situ* reduction of LDH flakes

LDO samples obtained by pre-calcination of the LDHs in the *in situ* XRD cell heated to 750 °C in Ar were used for the reduction procedure. There are two ways to reduce the LDOs. The first one is to reduce the catalyst from room temperature to 880 °C with a H_2 flow rate of 5 mL min^{-1}. The diffraction patterns were recorded at different temperatures, typically at intervals of 40 °C. The other one is that the diffraction patterns were recorded continuously at a scanning rate of 5.3° min^{-1} when the catalyst was maintained at 750 °C. The scans were performed over a 2θ range from 5° to 85°.

2.4. LDH flake reduction

The as-prepared LDHs were distributed on a quartz boat which was placed at the center of a horizontal quartz tube (inner diameter of 25 mm). The quartz tube was then inserted into a furnace and heated to 750 °C in Ar atmosphere at a flow rate of 115 mL min^{-1}. When reaching 750 °C, H_2 with a flow rate of 25 mL min^{-1} was introduced into the system to reduce the

calcined LDHs. The reduction was maintained for 0.5, 5, 30 and 60 min, respectively, and then the samples were cooled to room temperature under Ar protection.

2.5. CNT formation on LDH catalysts

Samples LDH-I–LDH-VI were used as the catalyst precursors to synthesize CNTs with a CVD method and the apparatus was the same as for the reduction process of LDHs. About 20 mg LDH catalysts were used for each sample. The reactor was heated to 750 °C at atmospheric pressure with Ar as the carrier gas. Then a mixed gas (H_2/C_2H_4) was introduced into the reactor with a flow rate of 25/20 mL min^{-1}. The CVD growth was maintained for 1 h at 750 °C before the furnace was cooled to room temperature under Ar protection. The as-grown products were then collected for further characterization.

2.6. Characterizations

The morphology of the LDH flakes and the as-grown CNT products was characterized using a JSM 7401F scanning electron microscope (SEM) operated at 3.0 kV. Energy dispersive spectrometer (EDS) analysis was carried out using a JSM-7401F apparatus at the accelerating voltage at 15.0 kV with the analytical software INCA. The formula of the FeMgAl LDHs can be expressed as $[Mg_{1-x-y}Fe_xAl_y(OH)_2](CO_3)_{(x+y)/2}\cdot mH_2O$ based on the charge balance. Once the relative amounts of Fe, Mg, and Al elements were confirmed, x and y in the formula were deduced and the molecular formula was available. A JEM 2010 high-resolution transmission electron microscope (TEM) operated at 120.0 kV was employed to detect the size and density of the Fe NPs in the LDO flakes and also the morphology and diameter of the CNT products. The scanning transmission electron microscopy (STEM) and high-angle annular dark-field-STEM (HAADF-STEM) images of the samples were collected on a FEI Tecnai G2 F20TEM. Thermogravimetric (TG) analysis was carried out using a Mettler Toledo TGA/DSC-1. A mass spectrometer (MS) was combined with the TG reactor to probe the real time pyrolysis products in the calcination process of LDHs. The BET specific surface area of the samples was measured by N_2 adsorption/desorption using an Autosorb-IQ2-MP-C system. Tests of H_2-temperature programmed reduction (TPR) of the LDO catalysts were conducted using a fixed-bed continuous flow microreactor (Quadrasorb ChemBET). The ramp rate of temperature was 10 °C min^{-1}. The change of hydrogen signal was monitored by on-line GC (Shimadzu GC-8A) with a TCD detector. The LDO catalyst precursor was first flushed by an Ar (of 99.999% purity, 20 sccm) stream at 673 K for 60 min to clean its surface, and then cooled down to room temperature, followed by switching to a N_2-carried 5.24 vol% H_2 gaseous mixture (20 sccm) as the reducing gas to start the TPR observation.

3. Results and discussion

3.1. Calcination of LDHs

The formation of metal NPs from LDHs always involves the high-temperature calcination of LDHs at the first step, which leads to the formation of their corresponding LDOs. Therefore, understanding the structural evolution process from LDHs to LDOs during the calcination is very important for the investigation of metal NP formation from LDHs. Herein, FeMgAl LDHs were taken as an example to investigate the calcination process of LDHs. Typical morphology of the FeMgAl LDH (LDH IV: $[Mg_{0.58}Fe_{0.11}Al_{0.31}(OH)_2](CO_3)_{0.21}\cdot mH_2O$) flakes is shown in Fig. 1, which illustrates that the LDHs are hexagonal flakes with a lateral size of 1–2 μm and a thickness of *ca.* 20 nm. When calcined from 30 to 1000 °C under N_2 atmosphere, five mass-loss regions are observed in the TGA profile of the FeMgAl LDHs (Fig. 1b). The first weight loss region around 102 °C with a weight loss of 3.1% corresponds to the evaporation of free water in the LDH flakes. When the temperature rises up to around 191 °C, the release of physisorbed and interlayer water molecules (as shown in the water profile determined using the MS in Fig. S1†), which can be expressed as:

$$[Mg_{1-x-y}Fe_xAl_y(OH)_2](CO_3)_{(x+y)/2}\cdot mH_2O \rightarrow [Mg_{1-x-y}Fe_xAl_y(OH)_2](CO_3)_{(x+y)/2} + mH_2O \quad (1)$$

causes a weight loss of 12.2%. The third weight loss region with a weight loss of 9.5% appearing at around 289 °C resulted from the decomposition of OH^- in the positively charged layers of LDH flakes. The release of water molecules from the pyrolysis products of the OH^- decomposition (both HO–M^{2+}–OH and HO–M^{3+}–OH) in the positively charged layers of LDH flakes can also be determined by the water profiles recorded using the MS (Fig. S1†). This can be described as:

$$[Mg_{1-x-y}Fe_xAl_y(OH)_2](CO_3)_{(x+y)/2} \rightarrow [Mg_{1-x-y}Fe_xAl_yO](CO_3)_{(x+y)/2} + H_2O \quad (2)$$

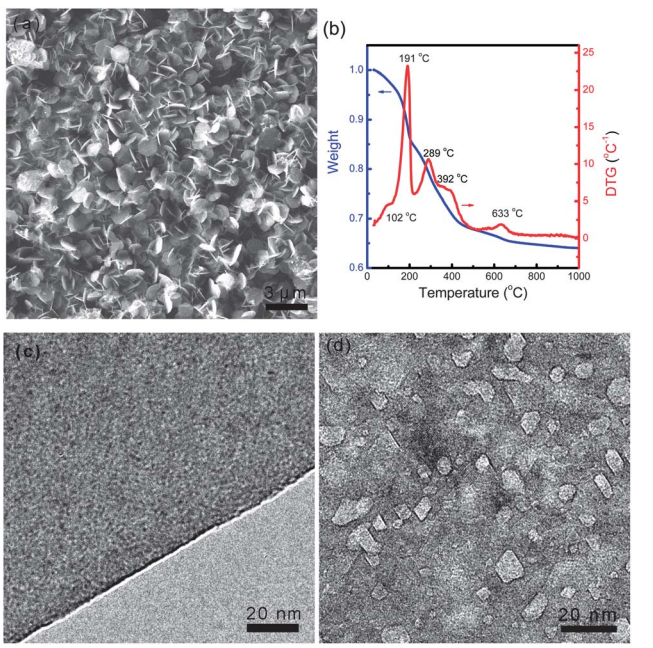

Fig. 1 (a) SEM image, (b) TG/DTG curves, and (c) TEM image of raw FeMgAl LDH-IV flakes; (d) TEM image of calcined LDO flakes.

A weight loss of 7.5% around 392 °C can be explained by the decomposition of CO_3^{2-} in the interlayer spaces of LDH flakes, in accordance with the MS spectrum of CO_2 in Fig. S1.† This can be illustrated as:

$$[Mg_{1-x-y}Fe_xAl_yO](CO_3)_{(x+y)/2} \rightarrow Mg_{1-x-y}Fe_xAl_yO_{(2+x+y)/2} + (x/2 + y/2)CO_2 \quad (3)$$

The last weight loss of 3.7% at around 633 °C is thought to be due to the removal of residual OH^- and CO_3^{2-} from the LDO flakes. This is consistent with the thermal evolution of the structure of a Mg–Al–CO_3 LDH reported by Yang *et al.*[23] After the calcination, it was observed that large quantities of pores in the mesoscale were formed on the LDO flakes (Fig. 1c and d).

In order to investigate the structural evolution of FeMgAl LDHs during the calcinations, *in situ* high temperature XRD analysis was introduced. As shown in Fig. 2a, four temperature regions can be identified based on the *in situ* XRD patterns, which are 30–170, 170–270, 270–390, and 390–750 °C, respectively. For the first temperature region of 30–170 °C, all the patterns are ascribed to the hydrotalcite-like layered structure (Phase I), which is consistent with that reported by Kanezaki.[22] In this temperature region, the intensities of the patterns are strong and the patterns remain almost unchanged with

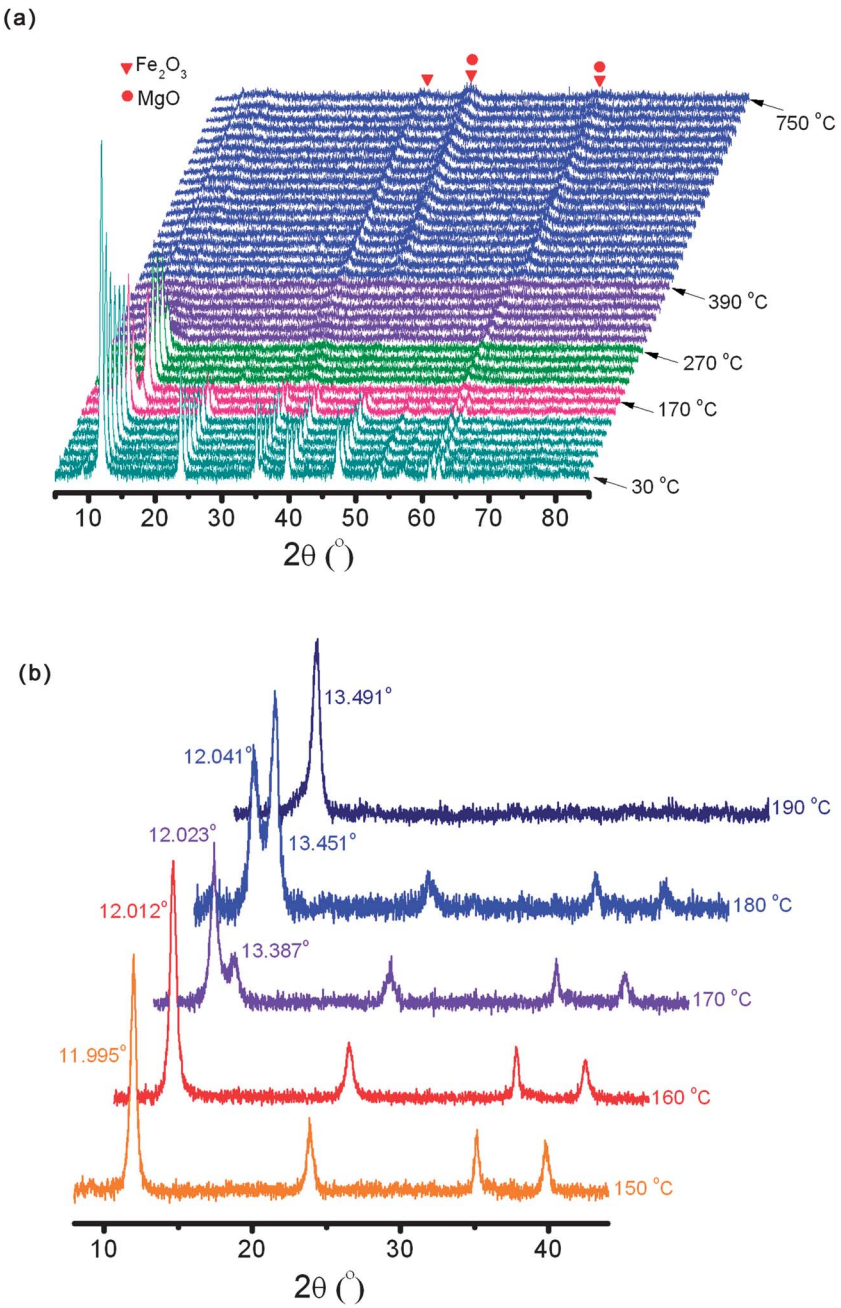

Fig. 2 (a) *In situ* XRD patterns of FeMgAl LDH-IV flakes as a function of temperature; the detailed patterns in the temperature range of 150–190 °C are displayed in (b).

increasing temperature below 170 °C, illustrating that the hydrotalcite-like structure of LDHs is well preserved. However, the basal spacing (for the (003) plane) of LDHs decreased from 0.744 to 0.737 nm as the temperature increased from 30 to 150 °C. The slight shrinkage of the layers of the FeMgAl LDHs can be attributed to the removal of some interlayer free water molecules because only free water was removed in this temperature region. The dramatic changes on the diffraction patterns between 150 and 190 °C are displayed in detail in Fig. 2b. The diffraction peak of the (003) plane further shifted from 11.995 to 12.012, to 12.023, and to 12.041°, indicating that the interlayer distance of the FeMgAl LDH further shrinked from 0.737 to 0.735, to 0.734, and to 0.733 nm when the temperature increased from 150 to 160, to 170, and to 180 °C, respectively. A small peak at 13.387° emerged when the temperature was raised to 170 °C, which became stronger with the increasing temperature. Meanwhile, the peak at ~12.0° weakened and completely disappeared when the temperature increased to 190 °C. This indicated that the structure of Phase I became obscure and another new phase (Phase II) with the basal spacing ~0.656 nm appeared at the temperature range of 170–190 °C. Considering the TGA results shown in Fig. 1b, the formation of Phase II can be attributed to the removal of interlayer water of the LDHs, which was consistent with the experimental reports by Yang *et al.*[23] However, the layered structure of LDHs was still preserved although the other XRD lines of Phase II weakened and the interlayer distance decreased in the former two regions. In the third temperature region 270–390 °C, the intensity of the peak at ~13.8° decreased sharply and finally disappeared, illustrating the collapse of the hydrotalcite-like structure of LDHs. This can be corresponded to the decomposition of OH^- in the positively charged layers of LDHs in this temperature region. In the fourth temperature region 390–750 °C, interlayer CO_3^{2-} began to decompose along with the removal of the residual OH^- and the formation of metal oxides, such as MgO and Fe_2O_3. The absence of the Al_2O_3 phase probably resulted from their amorphous structure. Therefore, it was concluded that the removal of interlayer H_2O, OH^-, and CO_3^{2-} in the LDHs occurred subsequently with the increasing temperature, and the cations diffused into a crystalline structure. Note that the different diffusivities of atoms in a diffusion couple (such as Mg–Al and Mg–Fe) caused a supersaturation of lattice vacancies, which involved the topotactic transformation of the LDHs into LDOs.[24] Consequently, the Kirkendall effect induced pores (which will be discussed in detail later) were distributed on the as-obtained LDO flakes at high temperatures (Fig. 1d and S2†). The BET specific surface areas (SSA) of the LDH and as-derived LDO were 83.5 and 149.5 $m^2\ g^{-1}$, and the pore volumes were 0.117 and 0.261 $cm^3\ g^{-1}$, respectively. The increase of both SSA and pore volume determined by N_2 sorption analysis was induced by the increase of mesopores (Fig. S2†).

3.2. Metal NP formation during the reduction of LDHs

Reduction of the FeMgAl LDO flakes leads to the formation of metal NPs, the process of which was investigated through the TPR and *in situ* XRD analysis. Four peaks were observed from the TPR profile of the FeMgAl LDO flakes (Fig. 3a). It has been reported that during the reduction process, ferric oxides are usually reduced to Fe NPs gradually from Fe_2O_3 to Fe_3O_4, to FeO, and to Fe in the corresponding temperature ranges of 300–470, 470–630 and 630–780 °C.[25] Due to their strong bonding, the reduction temperature of Fe^{3+} in the $MgFe_2O_4$ spinel phase always increased to 850–900 °C.[26] Taking into account that there is only one single cation of Fe^{3+} that can be reduced during the reduction of FeMgAl LDO flakes, the peaks at 460, 578, 703, and 875 °C in the TPR profile are ascribed to the consecutive reduction of Fe_2O_3 to Fe_3O_4, to FeO, to Fe, as well as the

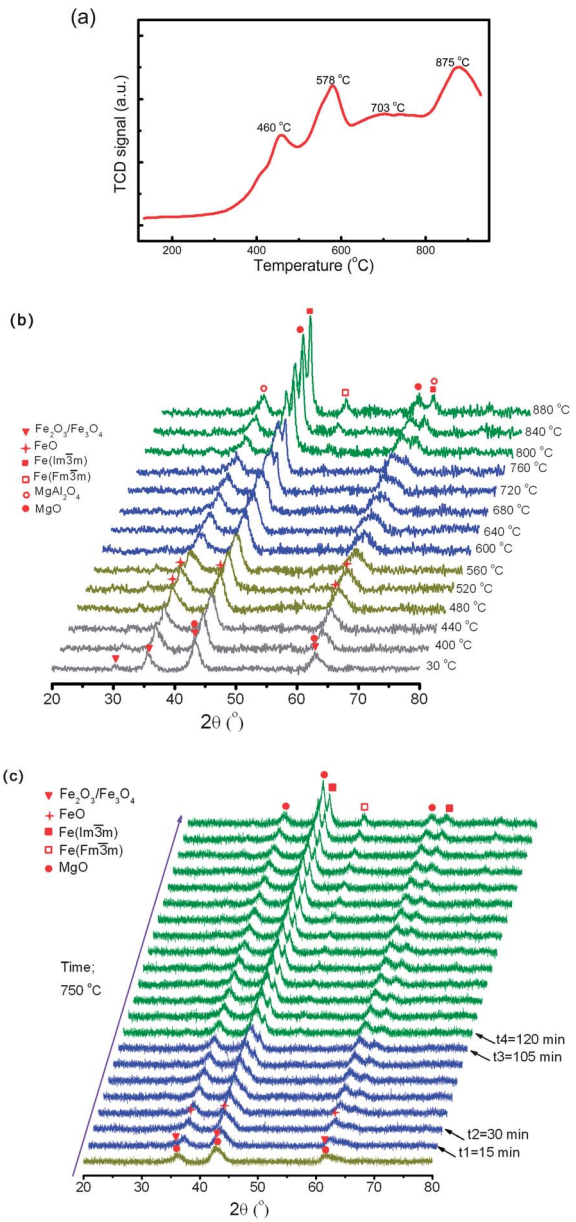

Fig. 3 (a) TPR curve of FeMgAl LDO flakes; XRD patterns of *in situ* reduction of LDO (b) during heating and (c) at a constant temperature of 750 °C.

reduction of Fe species in the spinels, respectively. The Fe species in the spinels were considered to be *in situ* formed during the TPR process at a temperature higher than 800 °C. The SSA and pore volume of reduced LDO were 100.4 $m^2 g^{-1}$ and 0.192 $cm^3 g^{-1}$, respectively.

Reduction of the FeMgAl LDO flakes was also *in situ* carried out in the X-ray diffractometer to investigate their structural evolution. The LDO flakes used were obtained after the *in situ* calcination of LDH-IV at 750 °C, and the *in situ* XRD patterns for the reduction process were collected from 30 to 880 °C under Ar/H_2 atmosphere. As shown in Fig. 2a, the calcined FeMgAl LDOs at 750 °C mainly consisted of MgO and Fe_2O_3. According to the TPR profile shown in Fig. 3a, the Fe_2O_3 phase cannot be reduced to Fe_3O_4 unless the temperature is higher than 350 °C. However, because the intrinsic peaks of the Fe_2O_3 and the Fe_3O_4 phase almost overlap, it is very hard to detect the changes of XRD patterns before the full transition of the Fe_2O_3 to the Fe_3O_4 phase. Therefore, no obvious changes were observed in the XRD pattern until the temperature reached 480 °C (Fig. 3b). When the reduction temperature was increased above 520 °C, the intrinsic peaks of the Fe_2O_3 phase at 30.2, 35.7, 43.4, and 57.4° gradually disappeared, while those for FeO at 36.3, 42.0, and 60.8° intensified with increasing temperatures, indicating the reduction of Fe_3O_4 and Fe_2O_3 into the FeO phase. When further increasing the temperature to above 600 °C, the intrinsic peak of the Fe phase at 44.6° appeared. This indicated the formation of Fe from the FeO phase by continuous reduction. The diffraction patterns of the FeO phase were weakened with the increasing reduction temperature and fully disappeared at the temperature of 800 °C. It was noticed that when the reduction temperature was higher than 760 °C, the diffraction peak of the spinel contributed by the $MgAl_2O_4$ phase at 65.2° appeared and began to be stronger with the increasing temperature. Formation of the Fe phase from the reduction of the $MgFe_2O_4$ spinel, which was reflected in the TPR profiles (Fig. 3a), was hard to be discerned yet due to the overlap between the diffraction peaks of $MgAl_2O_4$ and $MgFe_2O_4$ spinel phases. According to the top XRD profile in Fig. 3b, the reduced LDO flakes mainly consisted of Fe, $MgAl_2O_4$, and MgO phases.

In order to identify their reduction dynamics, the *in situ* calcined FeMgAl LDO flakes were directly reduced at 750 °C with increasing reduction time. The *in situ* diffraction patterns were recorded and are shown in Fig. 3c. With the introduction of H_2, Fe_2O_3 was converted firstly into Fe_3O_4 within the initial 15 min. Almost no changes in the diffraction patterns can be detected, which was attributed to the overlap between the characteristic peaks of the Fe_2O_3 and the Fe_3O_4 phase. When the reduction was carried out for $t_1 = 15$ min, the peaks of FeO at 36.3, 42.0, and 60.8° began to intensify, and fully disappeared at $t_3 = 105$ min. Interestingly, the characteristic peaks of metallic body-centered cubic Fe were with the initial appearance at $t_2 = 30$ min, and the original body-centered cubic Fe was partially transformed to face-centered cubic Fe at $t_4 = 120$ min. The face-centered cubic Fe is the dominant phase with large particle size at a reduction temperature of 750 °C.

3.3. Structure of the ultra-dispersed metal NPs on LDO flakes

The morphology of the Fe NPs formed after the calcination and reduction of FeMgAl LDHs was characterized by electron microscopies. The as-reduced FeMgAl LDO flakes can still retain the plate-like morphology of LDHs (Fig. 4). Large quantity of mono-dispersed and uniformly distributed NPs can be observed on the reduced FeMgAl LDO flakes. The composition of these NPs was confirmed by the HAADF-STEM image and EDS mapping (Fig. 5). The EDS mappings of Mg, Al, and O elements were almost overlapped, and the NPs uniformly distributed on the whole flakes were demonstrated to be mainly Fe NPs. Most of the Fe NPs were with a size of 10–25 nm. However, a very tiny iron phase with a diameter of *ca.* 1 nm can also be determined by checking the HAADF-STEM images carefully.

To understand the relationship between the Fe NPs and LDO flakes, the cross-section of the LDO flakes reduced at 900 °C for 30 min was carefully investigated by TEM. It was noticed that the lamellar structure of LDHs was still well preserved after the removal the OH^- and CO_3^{2-} by such a strong calcination at 900 °C and 30 min reduction in H_2/Ar atmosphere (Fig. 6). It has been mentioned that the different diffusivities of metal atoms in the LDHs during calcination cause a supersaturation of lattice vacancies,[24,27] which leads to a condensation of extra vacancies in the form of "Kirkendall voids" close to the interface (Fig. 1d, 6a, and 7a). With the introduction of H_2, the O atoms bonded with Fe cations preferred to be removed, and the diffusing rate of Fe atoms will be significantly accelerated. Compared with Fe cations, the reduced Fe atoms exhibited very weak metal–support interaction. As a result, the nulvalent Fe atoms rapidly conjoined into Fe NPs with a size of 8–15 nm. Some of the Fe NPs were embedded on the surface of the LDO flakes with part of them exposed to air (Fig. 6a), while others were totally embedded into the layered matrix with the (111) plane of the $MgAl_2O_4$ spinel phase parallel to the (110) plane of Fe NPs (Fig. 6b–d). The full encapsulation of reduced Fe NPs by

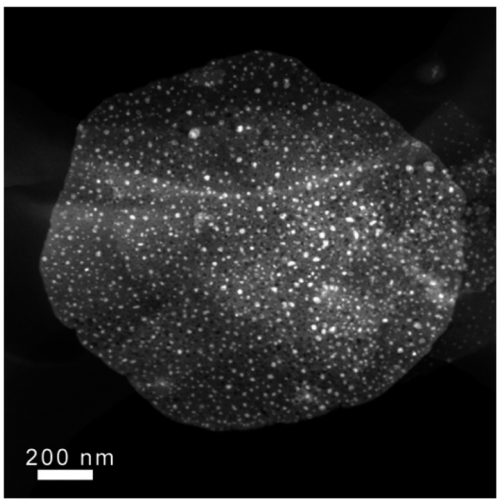

Fig. 4 STEM image of Fe distributed on LDO flakes.

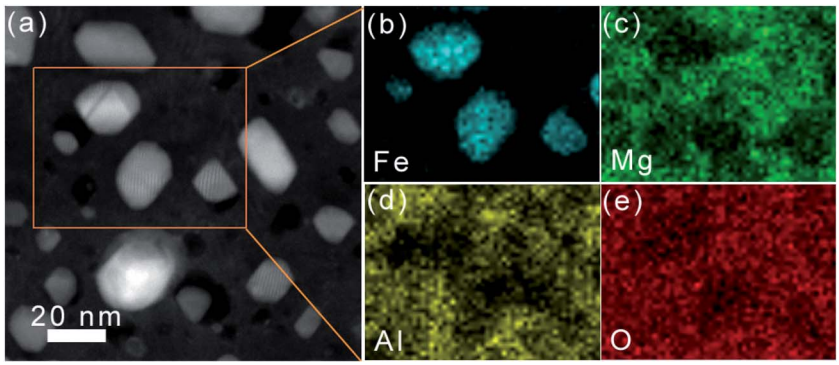

Fig. 5 High-angle annular dark-field (HAADF)-STEM image (a) and Fe, Mg, Al, and O mappings (b–e) of the FeMgAl LDO from LDH-IV flakes reduced at 750 °C for 30 min.

the spinel successfully prevented them from being oxidized when exposed to air (Fig. 6c and d). However, the exposed Fe NPs were easily oxidized into Fe_2O_3 when the reduced LDO flakes were exposed to air, and the as-obtained Fe_2O_3 NPs with well crystallization will still be embedded on the spinel substrates (Fig. 6e). As shown in the high resolution TEM image (Fig. 6f), a Fe_2O_3 NP with $d_{(320)} = 0.232$ nm and $d_{(040)} = 0.208$ nm was partially embedded into the LDO matrix.

Interestingly, the LDO flakes exhibit good crystallinity even though there are large quantities of Kirkendall voids distributed among the flakes. As shown in Fig. 7a, perfect alignment of the (111) direction of the $MgAl_2O_4$ spinel was unambiguously detected in large area. Such $MgAl_2O_4$ spinels with their common crystallographic orientations directly combining together to form larger ones were called as oriented attachment. The oriented-attachment assembly of primary units leads to the formation of mesocrystals/nanocrystals with irregular shapes. On the upper-right of Fig. 7a, the $MgAl_2O_4$ spinel phase with $d_{(220)} = 0.289$ nm and $d_{(202)} = 0.289$ nm can be observed. The fast Fourier transform (FFT) pattern was also shown with the [1−1−1] crystal axis, which was in good agreement with the cross-sectional image shown as Fig. 6c. A Moiré pattern from a different region in which the inset FFT pattern revealed a two-layer packing with a relative rotational angle of 14° is shown in Fig. 7b. Two individual atomic layers were reconstructed by masking the FFT pattern from this area (pink line). The size of the Moiré pattern was around 6×10 nm^2, while a routine single spinel phase can be detected at the lower-right of Fig. 7b. Therefore, the packing of spinel phases in the LDO flake is very complicated, in which MgO, $MgAl_2O_4$ spinel, and embedded Fe NPs can be found, which is consistent with the XRD results shown in Fig. 3.

3.4. Tuning the areal density of the ultra-dispersed NPs on LDO flakes

To obtain ultra-dispersed metal NPs with controllable size and areal density, a spectrum of FeMgAl LDHs with different Fe contents were synthesized (Table 1). After the calcination and reduction at Ar/H_2 atmosphere at 750 °C for 30 min, Fe NPs, as

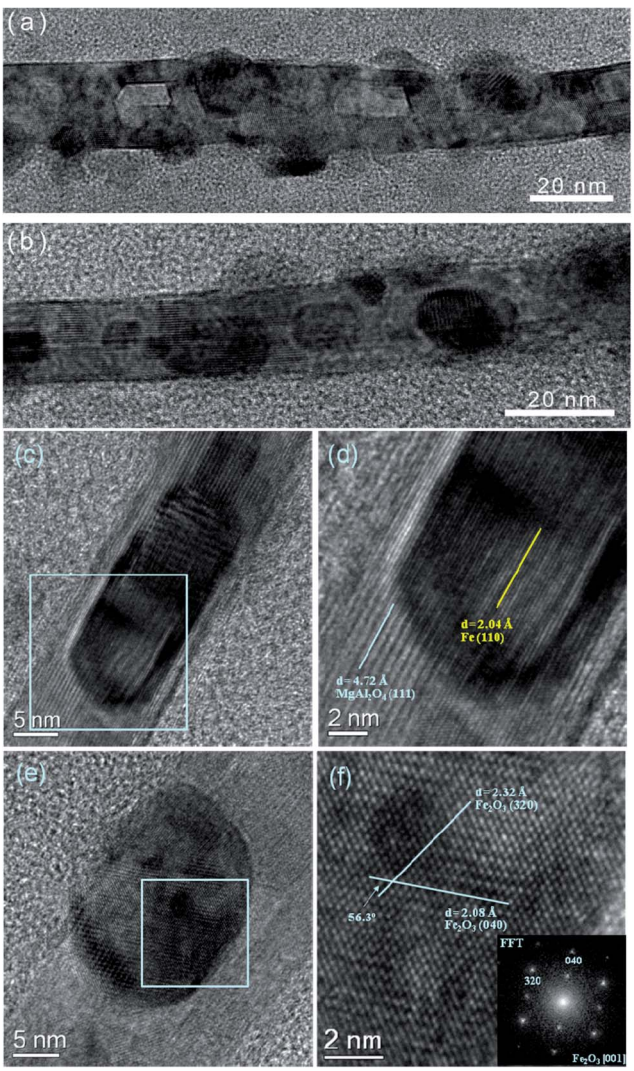

Fig. 6 TEM and high resolution TEM images of the cross-sections of the FeMgAl LDO flakes reduced at 900 °C. Both the Kirkendall voids and Fe NPs can be found in (a). The Fe NPs embedded in the LDO flake completely (b–d) or embedded on the LDO matrix (b, e and f); (d) and (f) are the enlarged images of the rectangular parts in (c and e), respectively. The catalyst NPs embedded on the LDO matrix have been oxidized into Fe_2O_3 NPs.

well as some Kirkendall voids, were distributed on all the as-obtained FeMgAl LDO flakes. TEM images of these reduced LDOs from LDH I–VI are shown in Fig. 8. Large quantities of Kirkendall voids with a size of 3–10 nm were observed to be distributed uniformly among the whole flake for all the LDOs. In contrast, the size and areal density of Fe NPs increased with the rising of Fe content in the LDH precursors. When the content of Fe was less than 7.9 wt% (LDH-I and LDH-II), there were only a few tiny Fe NPs on the corresponding reduced LDO flakes (Fig. 8a and b). However, the areal density of Fe NPs increased nearly 5 times (from 0.39×10^{13} to 1.8×10^{14} m^{-2}) when the Fe content was raised from 2.5 to 4.9 wt%. When the Fe content was further increased to 12.9 and to 25.5 wt% (LDH-IV and LDH-V), Fe NPs with tetrahedron/octahedral shapes uniformly formed on the LDO flakes can be observed (Fig. 8d and e). Furthermore, when the Fe content was increased to 32.3 wt% (LDH-VI), apparent aggregation of Fe NPs occurred for they were with a much larger average size of 15.2 nm (Fig. 8f). As shown in Table 1, both the average size and areal density of Fe NPs monotonously increased with the increasing Fe content in the LDH precursors. This can be well explained by the fact that both the particle migration and Ostwald ripening contributed to large metal NPs.

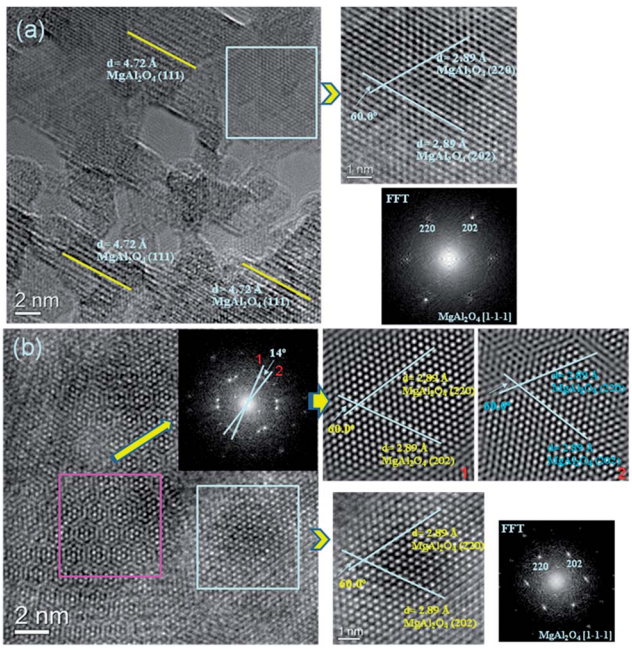

Fig. 7 (a) Typical high resolution TEM image of the LDO flake with nanoscale holes formed through the Kirkendall effect. (b) The Moiré pattern of LDO flake from a different region in which the inset FFT pattern reveals a two-layer packing with a relative rotational angle of 14°.

Among the various operation parameters to mediate the formation of Fe NPs from LDHs, the reduction time and temperature were investigated to monitor the kinetics. Typically, LDH-IV ($[Mg_{0.58}Fe_{0.11}Al_{0.31}(OH)_2](CO_3)_{0.21}\cdot mH_2O$) was calcined and then reduced by H_2 for different times of 0.5, 5, 30, and 60 min. TEM images of the reduced samples shown in Fig. 9 illustrated that in the initial period, the Fe NPs tended to become larger and more uniform while their density increased gradually with the prolonged reduction time till the reduction time was up to 30 min. When further reduction was carried out to 60 min, the size distribution of Fe NPs turned out to become wider with their density decreased to almost a half. This can be on account of the Ostwald ripening of the metal NPs. Statistical results of the density and average size of Fe NPs with different reduction times are provided in Table 2. In addition, we also compared the LDH-IV calcined and reduced at 750 °C with the same catalysts treated under a similar process at a higher temperature of 900 °C.[21] It was noticed that with the improved temperature, there were less but larger Fe NPs formed in the LDO flakes due to their decreased density but augmented size under the same reduction time (Table 2). This indicated that both the particle migration and Ostwald ripening became dominant at a higher temperature. Therefore, the high temperature can facilitate the reduction of Fe oxides and render the as-obtained Fe NPs more mobilizable, which sped up their aggregation.

3.5. Architectured CNT formation on metal NP catalysts with tunable areal density

The as-reduced LDO flakes with different Fe contents after reduction at 750 °C for 30 min were employed as the catalysts for CNT growth by routine CVD. The reason why we selected CNT growth as the probe reaction to evaluate the catalytic performance of the monodisperse metal NP catalysts is that the growth of CNTs can be directly correlated with the metal NP catalysts and the growth history was recorded.[28]

As shown in Fig. 10, only entangled CNTs can be obtained when the Fe content was low, *i.e.* for LDH-I and LDH-II

Table 1 A family of FeMgAl LDHs with different Fe contents and the densities and sizes of the Fe NPs formed on the corresponding reduced FeMgAl LDO flakes

Sample notation	Formula	Fe content (wt%)	Density (m^{-2})	Size (nm)
LDH-I	$[Mg_{0.64}Fe_{0.02}Al_{0.34}(OH)_2](CO_3)_{0.18}\cdot mH_2O$	2.5	3.9×10^{13}	—
LDH-II	$[Mg_{0.58}Fe_{0.04}Al_{0.38}(OH)_2](CO_3)_{0.21}\cdot mH_2O$	4.9	1.8×10^{14}	—
LDH-III	$[Mg_{0.62}Fe_{0.06}Al_{0.32}(OH)_2](CO_3)_{0.19}\cdot mH_2O$	7.3	5.5×10^{14}	—
LDH-IV	$[Mg_{0.58}Fe_{0.11}Al_{0.31}(OH)_2](CO_3)_{0.21}\cdot mH_2O$	12.9	1.2×10^{15}	11.2
LDH-V	$[Mg_{0.47}Fe_{0.24}Al_{0.29}(OH)_2](CO_3)_{0.265}\cdot mH_2O$	25.5	1.5×10^{15}	14.2
LDH-VI	$[Mg_{0.43}Fe_{0.32}Al_{0.25}(OH)_2](CO_3)_{0.285}\cdot mH_2O$	32.3	2.1×10^{15}	15.2

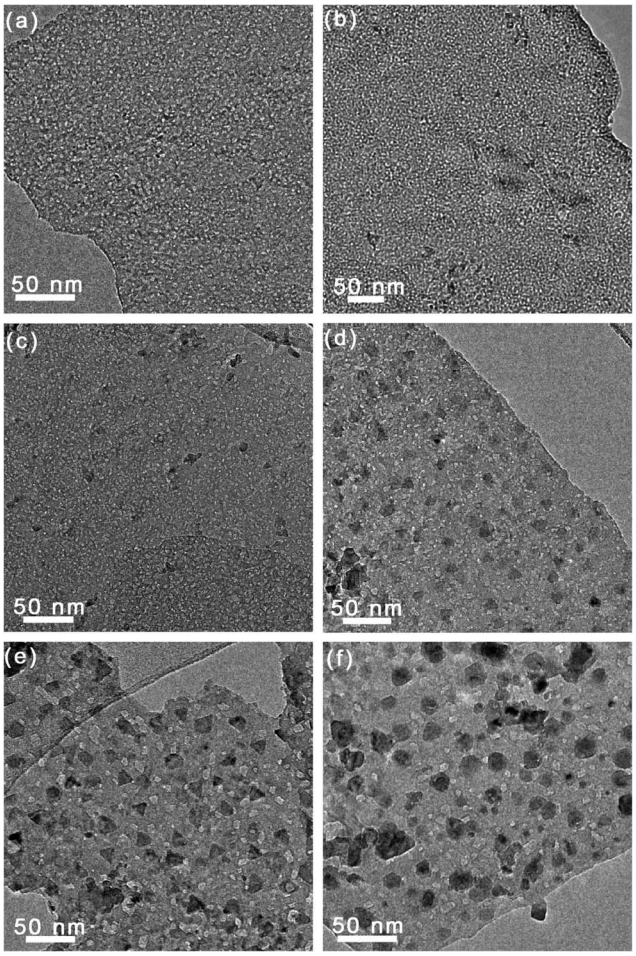

Fig. 8 TEM images of Fe NPs formed on the series of the FeMgAl LDOs reduced at 750 °C for 30 min, corresponding to (a) LDH-I, (b) LDH-II, (c) LDH-III, (d) LDH-IV, (e) LDH-V and (f) LDH-VI.

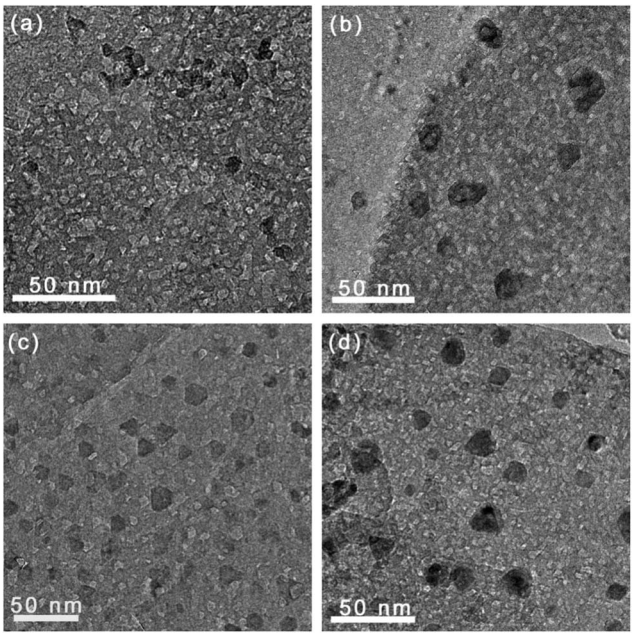

Fig. 9 TEM images of Fe NPs on the FeMgAl LDO flakes (corresponding to LDH-IV) at 750 °C for (a) 0.5 min, (b) 5 min, (c) 30 min, and (d) 60 min.

Table 2 Effects of reduction time and temperature on the density and size of the Fe NPs on the reduced FeMgAl LDO flakes corresponding to LDH-IV

	Density (m^{-2})		Size (nm)	
Time (min)	750 °C	900 °C	750 °C	900 °C
0.5	4.7×10^{14}	—	5.6	—
5	9.1×10^{14}	5.7×10^{14}	11.8	16.6
30	1.2×10^{15}	5.26×10^{14}	11.2	19.0
60	7.3×10^{14}	5.31×10^{14}	15.1	25.6

(Fig. 10a). When the Fe content increased to 7.3 wt% (LDH-III), short aligned CNTs were available (Fig. 10b). This can be attributed to the synchronous growth of CNTs from the high-density Fe NPs. Such phenomenon has been widely observed in aligned CNT formation on wafer and quartz sheet.[29–31] With the further increase of Fe content and the corresponding density of monodisperse Fe NPs (LDH IV–VI), it was noticed that the as-grown aligned CNTs from LDO flakes were self-organized into a double-helical structure. The relationship between the morphology of the as-grown CNTs and the diameter and areal density of metal NP catalysts is plotted in Fig. 10d, together with the reported data for aligned CNT growth and entangled CNT formation on wafer. It can be found that entangled CNTs are the dominant products when the density of metal NP catalysts is low, while high density metal NPs bring the self-organization of the as-grown CNTs into an aligned form. With further increase of the density of metal NP catalysts, the aligned CNTs in double-helical morphology will be available. It is well known that CNTs are a kind of typical chiral nanomaterials. When grown on a very light LDO flake, the as-obtained CNTs exert stresses that rotate, twist, and bend small sections of the catalyst during growth. However, the rotation of individual CNTs will be impeded by neighboring CNTs in the as-grown CNT arrays, leading to an internal rotation stress, which has been confirmed by Raman spectra and electron microscopy images in the previous reports.[29,32] When two CNT strands oppositely grow on a LDO flake with their two tips under space confinement, the as-grown aligned CNTs with the same-handed rotation will coil on themselves in order to release their internal stress and achieve a more stable morphology by self-organization, which finally leads to the formation of the CNT-array double helix.[18,32,33] The density of metal NP catalysts plays a key role for the self-assembly of aligned CNTs into a double-helix structure for the reason that internal rotation stress contributed from a large number of growing CNTs should be over a critical value before it can be self released. In the area of aligned CNT formation on the phase diagram, the high density catalysts are efficient for CNT array growth, but the internal rotation stress derived from CNT growth is not intense enough to lift and twist the catalyst flake. Consequently, aligned CNTs, not double helical CNTs, were available when the growth time was extended.

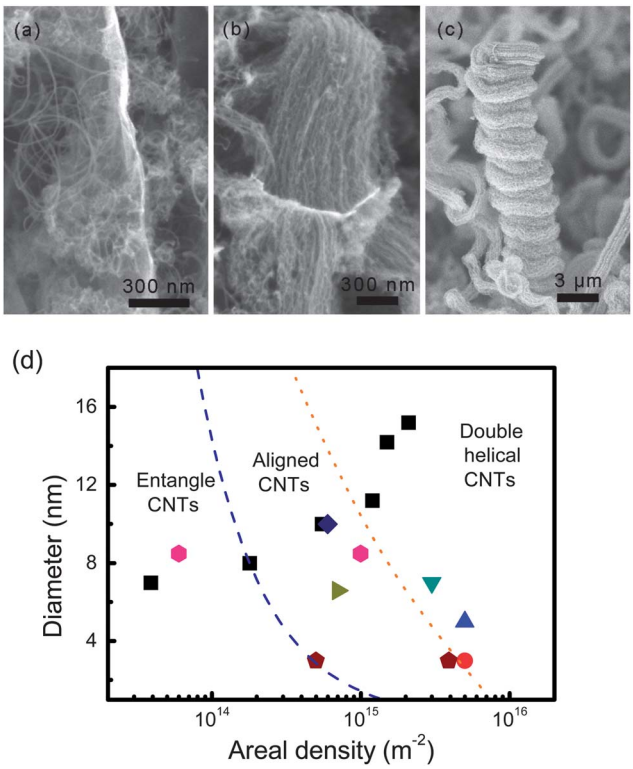

Fig. 10 (a) Entangled CNTs grown on LDH-I, (b) aligned CNTs grown on LDH-III, and (c) double helical aligned CNTs grown on LDH-V. (d) The phase diagram of CNTs grown on flat/flake substrates with different catalyst densities and sizes. Data source: square box ■: our result; round ●: ref. 37; upper triangle ▲: ref. 18; lower triangle ▼: ref. 21; right triangle ►: ref. 38; diamond ♦: ref. 39; pentagon ⬟: ref. 30; and hexagon ⬢: ref. 40.

Besides, the size of the metal NP catalyst also plays an important role in the morphology of the as-grown CNTs. Generally, small-sized metal NPs always required a much larger density to induce the morphology transformation, as shown in Fig. 10d. For instance, the average diameters of the CNTs grown from LDH IV, V, and VI were 5.56, 6.82, and 10.23 nm, respectively. The aligned single walled CNTs required active working tiny metal NPs in very high density, however, the metal NPs prefer to sinter into large NPs or deactivation by carbon coating. The ways to guarantee the working metal NPs in high density for architectured CNT formation, such as H_2O/CO_2 addition,[34] nanolaminate Fe–Al_2O_3 catalyst design,[35] and plasma pretreatment,[36] were very efficient to promote aligned CNT formation. The alignment of CNTs in the array is also dependent on the catalyst density and their uniformity because of a crowding effect from neighboring CNTs, that is, the increasing confinement of CNTs with increased density.[30] If the substrate is very heavy (*e.g.* wafer, quartz), aligned CNTs, not double helical CNTs, are grown out. Therefore, the double helical region in the current phase diagram should be updated as aligned CNTs when the weight of the substrate was very large. The density of working catalysts for CNT formation is the key to govern the formation of architectured CNTs. However, the ratio of active metal NPs among all metal NPs formed for efficient growth of CNTs is yet unknown, and it is hard to reveal the true value of areal density of active metal NP catalysts. The 'precise' boundary between the each architectured CNTs needs to be further determined.

4. Conclusions

LDHs in which the metal cations were pre-dispersed at an atomic scale were used as precursors for monodisperse metal NPs with tunable density. An *in situ* study of the calcination and reduction processes of FeMgAl LDHs was carried out to probe the monodisperse metal NP formation from LDH precursors. The different diffusivities of atoms in a diffusion couple (such as Mg–Al and Mg–Fe) caused a supersaturation of lattice vacancies, which were distributed uniformly on the as-obtained LDO flakes after the high-temperature calcination. During the reduction, the O atoms bonded with Fe^{3+} were easy to be extracted and the mobility of Fe was greatly increased at high temperatures (>750 °C). Consequently, the migration of Fe atoms was significantly improved and the Kirkendall effect was enhanced, leading to the formation of ultra-dispersed Fe NPs embedded on or in the LDO flakes. The areal density of the as-prepared Fe NPs on LDOs can be well mediated ranging from 0.039 to 2.1 × 10^{15} m^{-2} by adjusting the Fe content in the LDH precursors, the reduction time and temperature. When the metal NP catalysts embedded on the LDO flakes were adopted for the growth of CNTs, morphology transformation of the as-grown CNTs from entangled CNTs to aligned CNTs, and to CNT-array double helices was observed with the increase of areal metal NP density. The current calcination and reduction of LDH precursors were effective for the preparation of very high-density, monodisperse embedded metal NP catalysts, which is of paramount importance for heterogeneous catalysis and materials science. In addition, such *in situ* XRD together with TPR and atomic resolution TEM investigation strategy offers opportunities for characterizing the dynamic of metal NP formation with a high-precision time-resolved phase structure, which is crucial for probing dynamic changes on metal species and understanding their reactivity. This approach may also be applicable to systems using other functional nanomaterials with phase transition metals as the working catalysts, electrodes, and drugs.

Acknowledgements

The work was supported by the Foundation for the China National Program (no. 2011CB932602) and Natural Scientific Foundation of China (no. 21306102). Dang Sheng Su and Bingsen Zhang acknowledge the financial support from NSFC of China (21133010, 21203215) and MOST (2011CBA00504).

References

1 Q. Zhang, I. Lee, J. P. Ge, F. Zaera and Y. D. Yin, *Adv. Funct. Mater.*, 2010, **20**, 2201.
2 A. La Torre, M. D. Gimenez-Lopez, M. W. Fay, G. A. Rance, W. A. Solomonsz, T. W. Chamberlain, P. D. Brown and A. N. Khlobystov, *ACS Nano*, 2012, **6**, 2000.

3 M. K. Samantaray, J. Alauzun, D. Gajan, S. Kavitake, A. Mehdi, L. Veyre, M. Lelli, A. Lesage, L. Emsley, C. Coperet and C. Thieuleux, *J. Am. Chem. Soc.*, 2013, **135**, 3193.

4 J. C. Garcia-Martinez, R. Lezutekong and R. M. Crooks, *J. Am. Chem. Soc.*, 2005, **127**, 5097.

5 L. De Rogatis, M. Cargnello, V. Gombac, B. Lorenzut, T. Montini and P. Fornasiero, *ChemSusChem*, 2010, **3**, 24.

6 P. M. Arnal, M. Comotti and F. Schuth, *Angew. Chem., Int. Ed.*, 2006, **45**, 8224; I. Lee, Q. Zhang, J. P. Ge, Y. D. Yin and F. Zaera, *Nano Res.*, 2011, **4**, 115; I. Lee, M. A. Albiter, Q. Zhang, J. P. Ge, Y. D. Yin and F. Zaera, *Phys. Chem. Chem. Phys.*, 2011, **13**, 2449.

7 Z. W. Chen, M. Waje, W. Z. Li and Y. S. Yan, *Angew. Chem., Int. Ed.*, 2007, **46**, 4060.

8 W. F. Yan, S. Brown, Z. W. Pan, S. M. Mahurin, S. H. Overbury and S. Dai, *Angew. Chem., Int. Ed.*, 2006, **45**, 3614.

9 D. P. Yan, J. Lu, M. Wei, D. G. Evans and X. Duan, *J. Mater. Chem.*, 2011, **21**, 13128; Q. Wang and D. O'Hare, *Chem. Rev.*, 2012, **112**, 4124; S. He, Z. An, M. Wei, D. G. Evans and X. Duan, *Chem. Commun.*, 2013, **49**, 5912.

10 B. F. Sels, D. E. De Vos and P. A. Jacobs, *Catal. Rev.*, 2001, **43**, 443; G. Centi and S. Perathoner, *Microporous Mesoporous Mater.*, 2008, **107**, 3; D. P. Debecker, E. M. Gaigneaux and G. Busca, *Chem.–Eur. J.*, 2009, **15**, 3920; F. Z. Zhang, X. Xiang, F. Li and X. Duan, *Catal. Surv. Asia*, 2008, **12**, 253; Z. P. Xu, J. Zhang, M. O. Adebajo, H. Zhang and C. H. Zhou, *Appl. Clay Sci.*, 2011, **53**, 139; Z. An, J. He and X. Duan, *Chin. J. Catal.*, 2013, **34**, 225; J. L. Gunjakar, T. W. Kim, H. N. Kim, I. Y. Kim and S. J. Hwang, *J. Am. Chem. Soc.*, 2011, **133**, 14998.

11 P. Gao, F. Li, F. K. Xiao, N. Zhao, N. N. Sun, W. Wei, L. S. Zhong and Y. H. Sun, *Catal. Sci. Technol.*, 2012, **2**, 1447.

12 C. Qi, J. C. Amphlett and B. A. Peppley, *Int. J. Hydrogen Energy*, 2007, **32**, 5098; S. Kuhl, M. Friedrich, M. Armbruster and M. Behrens, *J. Mater. Chem.*, 2012, **22**, 9632.

13 L. He, Y. Q. Huang, A. Q. Wang, X. D. Wang, X. W. Chen, J. J. Delgado and T. Zhang, *Angew. Chem., Int. Ed.*, 2012, **51**, 6191.

14 Q. S. Wang, W. Ren, X. L. Yuan, R. M. Mu, Z. L. Song and X. L. Wang, *Int. J. Hydrogen Energy*, 2012, **37**, 11488.

15 X. J. Du, D. S. Zhang, L. Y. Shi, R. H. Gao and J. P. Zhang, *Nanoscale*, 2013, **5**, 2659.

16 M. Q. Zhao, Q. Zhang, X. L. Jia, J. Q. Huang, Y. H. Zhang and F. Wei, *Adv. Funct. Mater.*, 2010, **20**, 677.

17 L. Zhang, F. Li, X. Xiang, M. Wei and D. G. Evans, *Chem. Eng. J.*, 2009, **155**, 474.

18 Q. Zhang, M. Q. Zhao, D. M. Tang, F. Li, J. Q. Huang, B. L. Liu, W. C. Zhu, Y. H. Zhang and F. Wei, *Angew. Chem., Int. Ed.*, 2010, **49**, 3642.

19 M.-Q. Zhao, X.-F. Liu, Q. Zhang, G.-L. Tian, J.-Q. Huang, W. Zhu and F. Wei, *ACS Nano*, 2012, **6**, 10759.

20 Y. D. Li, J. L. Chen and L. Chang, *Appl. Catal., A*, 1997, **163**, 45; J. L. Chen, Q. Ma, T. E. Rufford, Y. D. Li and Z. H. Zhu, *Appl. Catal., A*, 2009, **362**, 1; I. Kvande, D. Chen, Z. Yu, M. Ronning and A. Holmen, *J. Catal.*, 2008, **256**, 204.

21 M. Q. Zhao, Q. Zhang, W. Zhang, J. Q. Huang, Y. H. Zhang, D. S. Su and F. Wei, *J. Am. Chem. Soc.*, 2010, **132**, 14739.

22 E. Kanezaki, *Inorg. Chem.*, 1998, **37**, 2588.

23 W. S. Yang, Y. Kim, P. K. T. Liu, M. Sahimi and T. T. Tsotsis, *Chem. Eng. Sci.*, 2002, **57**, 2945.

24 Y. D. Yin, R. M. Rioux, C. K. Erdonmez, S. Hughes, G. A. Somorjai and A. P. Alivisatos, *Science*, 2004, **304**, 711; Y. D. Yin, C. K. Erdonmez, A. Cabot, S. Hughes and A. P. Alivisatos, *Adv. Funct. Mater.*, 2006, **16**, 1389.

25 G. Munteanu, L. Ilieva and D. Andreeva, *Thermochim. Acta*, 1997, **291**, 171; M. Q. Zhao, Q. Zhang, J. Q. Huang, J. Q. Nie and F. Wei, *Carbon*, 2010, **48**, 3260.

26 J. M. Fernandez, M. A. Ulibarri, F. M. Labajos and V. Rives, *J. Mater. Chem.*, 1998, **8**, 2507.

27 H. J. Fan, M. Knez, R. Scholz, K. Nielsch, E. Pippel, D. Hesse, M. Zacharias and U. Gosele, *Nat. Mater.*, 2006, **5**, 627; H. J. Fan, U. Gosele and M. Zacharias, *Small*, 2007, **3**, 1660.

28 M. Q. Zhao, Q. Zhang, J. Q. Huang and F. Wei, *Adv. Funct. Mater.*, 2012, **22**, 675.

29 Q. Zhang, W. P. Zhou, W. Z. Qian, R. Xiang, J. Q. Huang, D. Z. Wang and F. Wei, *J. Phys. Chem. C*, 2007, **111**, 14638.

30 M. Xu, D. N. Futaba, M. Yumura and K. Hata, *ACS Nano*, 2012, **6**, 5837.

31 E. S. Polsen, M. Bedewy and A. J. Hart, *Small*, 2013, **9**, 2564.

32 M. Q. Zhao, Q. Zhang, G. L. Tian, J. Q. Huang and F. Wei, *ACS Nano*, 2012, **6**, 4520.

33 Y. Wang, J. Xu, Y. W. Wang and H. Y. Chen, *Chem. Soc. Rev.*, 2013, **42**, 2930.

34 K. Hata, D. N. Futaba, K. Mizuno, T. Namai, M. Yumura and S. Iijima, *Science*, 2004, **306**, 1362.

35 G. F. Zhong, J. H. Warner, M. Fouquet, A. W. Robertson, B. A. Chen and J. Robertson, *ACS Nano*, 2012, **6**, 2893.

36 C. Zhang, R. Xie, B. Chen, J. Yang, G. Zhong and J. Robertson, *Carbon*, 2013, **53**, 339.

37 M. Q. Zhao, J. Q. Huang, Q. Zhang, J. Q. Nie and F. Wei, *Carbon*, 2011, **49**, 2148.

38 X. B. Zhang, K. L. Jiang, C. Teng, P. Liu, L. Zhang, J. Kong, T. H. Zhang, Q. Q. Li and S. S. Fan, *Adv. Mater.*, 2006, **18**, 1505.

39 R. D. Bennett, A. J. Hart and R. E. Cohen, *Adv. Mater.*, 2006, **18**, 2274.

40 N. T. Alvarez, F. Li, C. L. Pint, J. T. Mayo, E. Z. Fisher, J. M. Tour, V. L. Colvin and R. H. Hauge, *Chem. Mater.*, 2011, **23**, 3466.

